Signal, Image and Video Processing (2020) 14:29–37
https://doi.org/10.1007/s11760-019-01520-6

ORIGINAL PAPER

Intravascular optical coherence tomography image segmentation based on Gaussian mixture model and adaptive fourth-order PDE

Pengyu Wang[1] · **Hongqing Zhu**[1] · **Xiaofeng Ling**[1]

Received: 13 March 2019 / Revised: 17 May 2019 / Accepted: 10 June 2019 / Published online: 19 June 2019

Abstract
The accuracy of the fibrotic plaque segmentation is vital in identifying the coronary artery stenosis. In this paper, we address an automated approach (APDE-GMM) for separating the fibrotic plaque area of intravascular optical coherence tomography (IV-OCT) images. Under this approach, an objective function consisting of a new energy functional with Rayleigh distribution and the negative log-likelihood function of Gaussian mixture model (GMM) is developed. Also, the study presents an adaptive diffusivity function where the gradient threshold can be associated to suppress the effect of speckle noise. The parameter estimation is carried out by the expectation–maximization technology. In addition, this paper derives a fourth-order partial differential equation (PDE) via Euler–Lagrange equation to obtain the optimal solutions. It has been compared to other segmentation approaches on synthetic and clinical IV-OCT images. The results demonstrate that APDE-GMM segmentates more accurately.

Keywords Fibrotic plaque · Optical coherence tomography · Partial differential equation · Gaussian mixture model · Image segmentation

1 Introduction

Intravascular optical coherence tomography (IV-OCT) image is an intracoronary detecting technique which has high resolution and low radiation. Perfect segmentation of the fibrotic plaque area in IV-OCT images can provide useful information of coronary artery stenosis. As a result, doctors could get a more reliable diagnostic of coronary atherosclerotic heart disease (CAD).

Relevant IV-OCT image segmentation methods have been widely reported in recent years. Zahnd et al. [1] segmented the fibrotic plaque via a front propagation scheme which runs in a 4D multi-parametric space to identify the healthy status. Segmentation IV-OCT using support vector machine (SVM) was found in the literature [2]. The theory of anisotropic diffusion was also investigated in IV-OCT image segmentation [3]. Celi et al. modeled fibrotic plaque using Ostu's method and mathematical morphology [4]. Recently, convolutional neural networks (CNN), such as ResNet50-V2, have been applied successfully to IV-OCT images with plaque [5]. These methods require a large number of images for training. In addition, finite mixture model (FMM) technique, for instance, Gaussian mixture model (GMM), Student's-*t* mixture model (SMM) have been addressed [6–9]. Some researches [6,10] incorporated pixel position information into GMM through Markov random field (MRF), so that their methods are highly resistant to noise. Cheriyan et al. [7] combined the independent component analysis (ICA) with GMM for unsupervised medical image segmentation. Due to the incorporation of ICA, the computation of their method was expensive. Although statistical methods have been widely applied to various image segmentation, no report has been found on detecting the fibrotic plaque from IV-OCT using FMM so far.

Due to the clinical IV-OCT images suffering from the heavy speckle noise, some researches apply partial differential equation (PDE) on IV-OCT images for denoising [11–16]. In [11], the fourth-order PDE with a nonlinear hyperbolic diffusion was used for eliminating the impact of noise. However, this approach converges slowly. Another PDE with two-dimension Gaussian filter was introduced in [12]. The work of [13] introduced an algorithm where a nonlinear hyperbolic diffusion-combined Gaussian kernel was

✉ Hongqing Zhu
hqzhu@ecust.edu.cn

[1] School of Information Science and Engineering, East China University of Science and Technology, Shanghai, China

utilized for image denoising, but it results in higher calculation cost. These researches show that the PDE-based denoising method can effectively remove noise while preserving image edge [14]. Reference [15] reported an improved algorithm using fourth-order PDE with edge noise interior (ENI). This method exhibits good robustness to different levels of speckle noise. But it needs to count the number of homogeneous pixels in the neighborhood, which is a hard work. Recently, Kumar et al. [16] proposed a PDE-based fuzzy c-mean (FCM) algorithm in order to assist in eliminating the effect of Poisson noise. Their method helps to get rid of the block artifact in the process of cell segmentation.

In this paper, we propose a hybrid framework for IV-OCT image segmentation. Comparing with other existing algorithms, this framework has the following properties: (1) this study develops a unsupervised image segmentation approach where the negative log-likelihood function of GMM is designed within the framework of a new energy functional with Rayleigh distribution; (2) the integrand of the proposed energy functional is divided into two parts: the likelihood function of Rayleigh distribution and the adaptive diffusivity function with respect to gradient; (3) it recommends applying adaptive diffusivity function with the gradient threshold to withstand the effect of speckle noise; (4) from the computational perspective, we derive a fourth-order PDE for iteratively finding the optimal solutions through Euler–Lagrange equation; (5) The M-step of EM algorithm is applied to optimize model parameters of GMM.

The rest of the article is organized as follows. A review of the GMM is introduced in Sect. 2. Section 3 describes the main concepts of our approach. Section 4 provides more details about its implementation. The experimental results could be found in Sect. 5, and conclusions are summarized in Sect. 6.

2 A review of GMM

In order to label the L pixels of an image into K parts, the GMM assumes that each observation x_i is independent of the label Ω_j. In this case, the density function of each x_i can be described by

$$f(x_i|\Pi,\Theta)=\sum_{j=1}^{K}\pi_{ij}g(x_i|\theta_j) \tag{1}$$

where $\Pi=\{\pi_{ij}\}$, $i=(1,2,\ldots,L)$, $j=(1,2,\ldots,K)$ is the set of prior probability, which satisfies the constraints

$$0\le\pi_{ij}\le 1 \quad\text{and}\quad \sum_{j=1}^{K}\pi_{ij}=1 \tag{2}$$

and π_{ij} indicates the possibility of the pixel x_i belongs to the jth label. In (1), $g(x_i|\theta_j)$ denotes the multivariate Gaussian probability density function (PDF) with mean μ_j and covariance Σ_j

$$g(x_i|\theta_j)=\frac{1}{(2\pi)^{1/2}}\frac{1}{|\Sigma_j|^{1/2}}\exp\left\{-\frac{1}{2}(x_i-\mu_j)^{\mathrm{T}}\Sigma_j^{-1}(x_i-\mu_j)\right\} \tag{3}$$

where θ_j represents the parameter set $\{\mu_j,\Sigma_j\}$, and $|\Sigma_j|$ is the determinant of Σ_j. Thus, the joint conditional PDF of observation data $X=(x_1,x_2,\ldots,x_L)$ can be modeled using

$$P(X|\Pi,\Theta)=\prod_{i=1}^{L}f(x_i|\Pi,\Theta)=\prod_{i=1}^{L}\sum_{j=1}^{K}\pi_{ij}g(x_i|\theta_j) \tag{4}$$

The parameters associated with the GMM are usually estimated using EM scheme. Therefore, one needs to maximize the following log-likelihood function of the GMM.

$$\begin{aligned}\mathscr{L}(X|\Pi,\Theta)&=\log P(X|\Pi,\Theta)\\&=\sum_{i=1}^{L}\log\left\{\sum_{j=1}^{K}\pi_{ij}g(x_i|\theta_j)\right\}\end{aligned} \tag{5}$$

3 Proposed method

In this section, a hybrid framework is proposed for IV-OCT image segmentation, which blends the fourth-order nonlinear PDE and GMM. We start by developing an adaptive speckle noise filter based on fourth-order PDE.

The speckle noise of IV-OCT images follows the Rayleigh distribution [17]. This problem is described as

$$p(u|\bar{u})=\frac{\pi u}{2\bar{u}^2}\exp\left(-\frac{\pi u^2}{4\bar{u}^2}\right) \tag{6}$$

where u and $\bar{u}$ are the restored and observed initial images with size of $m\times n$, respectively. In this case, the maximum likelihood estimate of u can be obtained by minimizing $p(u|\bar{u})$.

$$\mathscr{L}_1(u|\bar{u})=\ln p(u|\bar{u})=\ln(\pi u/2\bar{u}^2)-\pi u^2/4\bar{u}^2 \tag{7}$$

Based on this, the energy functional is defined as follows

$$J_1=E(u)=\int_{\Omega}\left[\mathscr{L}_1(u|\bar{u})+\lambda\varphi(|\nabla^2 u|)\right]\mathrm{d}\Omega \tag{8}$$

where λ is a regularization parameter, and ∇^2 stands for Laplacian operator. In Cartesian coordinates

$$\nabla^2 u = \frac{\partial^2 u}{\partial m^2} + \frac{\partial^2 u}{\partial n^2} \tag{9}$$

This paper would establish a function with respect to the smoothness of the image as implemented by $|\nabla^2 u|$. According to the physical theory of diffusion, the second term of the right-hand side of (8) is defined by

$$\varphi(s) = \int_0^s \phi(s) t \mathrm{d}t \tag{10}$$

where $s = |\nabla^2 u|$. This study defines an adaptive nonlinear diffusivity function, given by

$$\phi(s) = 1 / \left[1 + (\ln[(s/\eta(u))^3 + 1])^2\right] \tag{11}$$

Generally, the diffusivity function $\phi(s)$ is a monotonically decreasing function, since the idea is to reduce smoothing at edge where $|\nabla^2 u|$ is large. Following this, the gradient threshold $\eta(u)$ is defined as

$$\eta(u) = \alpha\,[\text{mean}\,(||\nabla u||) + \text{med}(||\nabla u||)] + \beta N \tag{12}$$

where $||\cdot||$ represents Euclidean distance, mean $||\nabla u||$ denotes the mean value of $||\nabla u||$, and med $||\nabla u||$ stands for the median value of $||\nabla u||$, β is a regularized parameter, and N is the number of iterations. In Fig. 1, we exhibit an experiment to compare the smoothing properties of classical Y–K diffusivity function [18] to ours. The diffusivity function of Y–K model is independent to iterations (see Fig. 1a). Figure 1b depicts the plots of our adaptive diffusivity function with parameters $\alpha = 0.5$, $\beta = 0.05$. These diffusivity functions are applied to noisy image that exists because of the speckle noise (intensity 5%). For fair comparison of the performance, the iteration number of two models is set equal. As shown in Fig. 1f, the proposed diffusion function achieves a better result with more noise removal, with our adaptive diffusivity function, each region could be smoothed well.

When constructing this adaptive diffusivity function, all the following items should be considered. (i) The diffusivity function $\phi(s)$ follows a downward trend with increasing of smoothing term $|\nabla^2 u|$ (Laplacian of u); (ii) as iteration increases, the plot of diffusivity function $\phi(s)$ moves down; (iii) at the beginning of iteration, image contained excessive noise, the higher diffusivity ought to be chosen in this case; (iv) as $|\nabla^2 u|$ increases, the impact of parameters N, α and β on diffusivity function $\phi(s)$ will be weakened, and $\phi(s)$ converges to zero. Again, we observe from Fig. 1 that our adaptive diffusivity function meets all these properties.

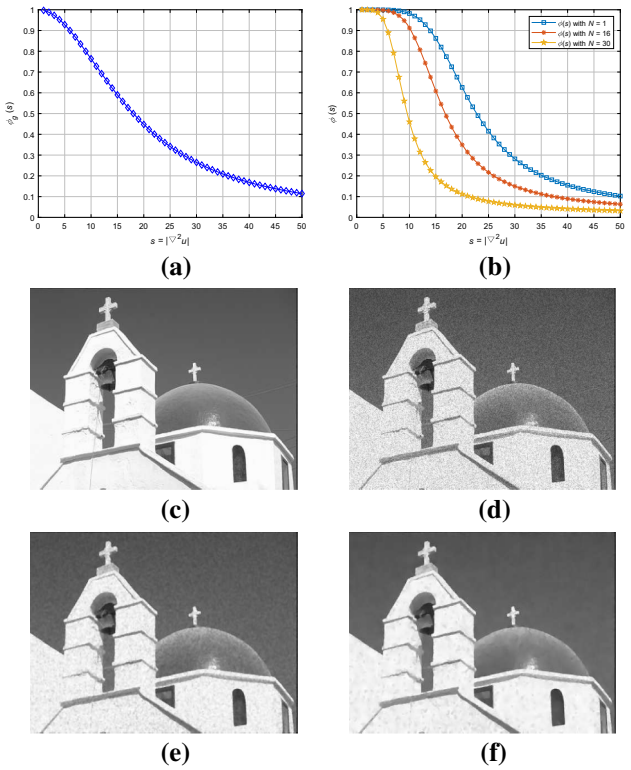

Fig. 1 Diffusivity function comparison, **a** diffusivity function of Y–K model; **b** proposed diffusivity function with $\alpha = 0.5$, $\beta = 0.05$; **c** original image; **d** noisy image (speckle noise, intensity 5%); **e** denoising using Y–K model; **f** denoising using proposed model

Since logarithm is a monotonically increasing function, we take the negative logarithm of the likelihood function as an energy function. By introducing the posterior probability z_{ij}, minimizing the negative log-likelihood function in (5) leads to minimizing the following expression

$$J_2 = -\sum_{i=1}^{L}\sum_{j=1}^{K} z_{ij}^{(t)} \left\{ \ln \pi_{ij} + \ln g(x_i|\theta_j) \right\} \tag{13}$$

where the posterior probability z_{ij} at the current iteration is

$$z_{ij}^{(t)} = \pi_{ij} g(x_i|\theta_j) / \sum_{k=1}^{K} \pi_{ik} g(x_i|\theta_j) \tag{14}$$

Generally, classical GMM cannot deal with noise properly. It is because GMM does not consider the spatial correlation of pixels. Speckle noise exists elsewhere in real IV-OCT images, so the fourth-order PDE based on Rayleigh distribution is introduced here. Finally, the APDE-GMM is implemented by minimizing the following objective function:

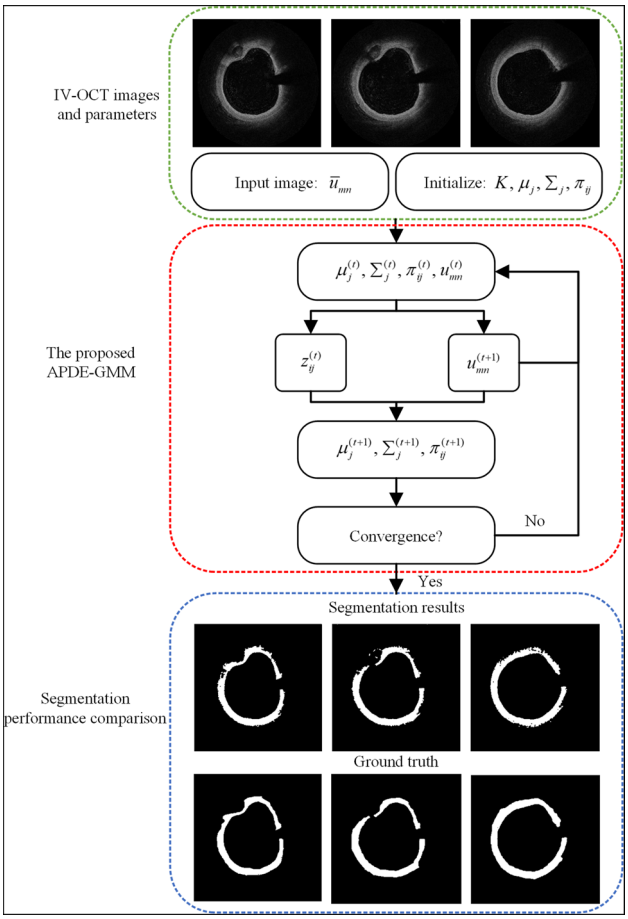

Fig. 2 The overall segmentation process using the APDE-GMM

$$J = J_1 + J_2 = \int_\Omega \left[\mathscr{L}_1(u|\bar{u}) + \lambda\varphi(|\nabla^2 u|)\right] \mathrm{d}\Omega - \sum_{i=1}^{L}\sum_{j=1}^{K} z_{ij}^{(t)} \left\{ \ln \pi_{ij} + \ln g(x_i|\theta_j) \right\} \tag{15}$$

where λ is a regularized parameter. As shown in Fig. 2, the fusion model illustrated here is an iterative strategy. It incorporates denoising and segmentation in a single produce.

4 Implementation issues

In the following, we discuss the numerical approximation of the proposed method. The proposed objective function J is the linear sum of the energy functional J_1 and the negative log-likelihood function J_2. Then, minimizing the objective function J in (15) is equivalent to minimizing J_1 and J_2, respectively. In this study, Euler–Lagrange equation and EM algorithm are, respectively, applied to minimize energy functional J_1 and the negative log-likelihood function J_2. Thus,

$$J = \int_\Omega \left[\mathscr{L}_1(u_{mn}|\bar{u}_{mn}) + \lambda\varphi(|\nabla^2 u_{mn}|)\right] d\Omega - \sum_{i=1}^{L}\sum_{j=1}^{K} z_{ij}^{(t)} \left\{ \ln \pi_{ij} - \frac{1}{2}\ln(2\pi) - \frac{1}{2}\ln|\Sigma_j| \right\} - \sum_{i=1}^{L}\sum_{j=1}^{K} z_{ij}^{(t)} \left\{ -\frac{1}{2}(x_i - \mu_j)^T \Sigma_j^{-1}(x_i - \mu_j) \right\} \tag{16}$$

The efficient implementation of the APDE-GMM depends on the correct estimation of the parameter u_{mn}. According to variational method, if an optimal estimation of u_{mn} exists, it satisfies the Euler–Lagrange equation. Based on this, from the objective function (16), we have

$$\frac{\pi u_{mn} - 2\bar{u}_{mn}^2}{2u_{mn}\bar{u}_{mn}^2} - \lambda\nabla^2\left[\phi(|\nabla^2 u_{mn}|)\nabla^2 u_{mn}\right] = 0 \tag{17}$$

This PDE may be solved numerically using a finite difference scheme. Letting $\gamma_{mn} = \phi(|\nabla^2 u_{mn}|)\nabla^2 u_{mn}$, the second term of left-hand side of (17) becomes

$$\lambda\nabla^2\left[\phi(|\nabla^2 u_{mn}|)\nabla^2 u_{mn}\right] = \lambda\frac{\gamma_{m+h,n} + \gamma_{m-h,n} + \gamma_{m,n+h} + \gamma_{m,n-h} - 4\gamma_{mn}}{h^2} \tag{18}$$

with

$$\gamma_{mn} = \phi\left(\frac{u_{m+h,n} + u_{m-h,n} + u_{m,n+h} + u_{m,n-h} - 4u_{mn}}{h^2}\right) \times \left(\frac{u_{m+h,n} + u_{m-h,n} + u_{m,n+h} + u_{m,n-h} - 4u_{mn}}{h^2}\right) \tag{19}$$

where h is step length. Considering that the problem of $||\cdot||$ is Euclidean distance, the function $\eta(u)$ of (12) becomes

$$\eta(u) = \alpha\left(\mathrm{mean}\left(\frac{\sqrt{(u_{m+h,n} - u_{m-h,n})^2 + (u_{m,n+h} - u_{m,n-h})^2}}{2h}\right) + \mathrm{med}\left(\frac{\sqrt{(u_{m+h,n} - u_{m-h,n})^2 + (u_{m,n+h} - u_{m,n-h})^2}}{2h}\right)\right) + \beta N \tag{20}$$

Taking $h = 1$, we have the numerical approximation about (17) in the following form

$$u_{mn}^{(t+1)} = u_{mn}^{(t)} - \Delta t\left(\frac{2\bar{u}_{mn}^2 - \pi u_{mn}^{(t)}}{2u_{mn}^{(t)}\bar{u}_{mn}^2} + \lambda\left(\gamma_{m+1,n}^{(t)} + \gamma_{m-1,n}^{(t)} + \gamma_{m,n+1}^{(t)} + \gamma_{m,n-1}^{(t)} - 4\gamma_{mn}^{(t)}\right)\right) \tag{21}$$

where

$$\gamma_{mn} = \phi(u_{m+1,n} + u_{m-1,n} + u_{m,n+1} + u_{m,n-1} - 4u_{mn}) \times (u_{m+1,n} + u_{m-1,n} + u_{m,n+1} + u_{m,n-1} - 4u_{mn}) \tag{22}$$

Next, we are going to discuss the optimization of parameters μ_j, Σ_j and π_{ij}. The EM technique is utilized to find the optimal parameters. To satisfy GMM, the observed data x is L-length 1D u_{mn}, here, $L = NM$. For mean μ_j, the optimal value of it occurs when the partial derivative of objective function J with respect to μ_j is zero

$$\frac{\partial J}{\partial \mu_j} = -\sum_{i=1}^{L} z_{ij} \left[\frac{x_i - \mu_j}{\Sigma_j} \right] = 0 \tag{23}$$

Eventually, we get the mean μ_j at the $(t+1)$ iteration step.

$$\mu_j^{(t+1)} = \sum_{i=1}^{L} z_{ij}^{(t)} x_i \Big/ \sum_{i=1}^{L} z_{ij}^{(t)} \tag{24}$$

Similarly, the estimation of covariance is worked out via Σ_j which satisfies

$$\frac{\partial J}{\partial \Sigma_j} = \sum_{i=1}^{L} z_{ij} \left[\frac{\sum_j - (x_i - \mu_j)(x_i - \mu_j)^T}{2\Sigma_j^2} \right] \tag{25}$$

Then, letting $\partial J / \partial \Sigma_j = 0$, the update of covariance Σ_j at the $(t+1)$ iteration is as follows

$$\Sigma_j^{(t+1)} = \sum_{i=1}^{L} z_{ij}^{(t)} (x_i - \mu_j^{(t+1)})(x_i - \mu_j^{(t+1)})^T \Big/ \sum_{i=1}^{L} z_{ij}^{(t)} \tag{26}$$

As for priori probability π_{ij}, we use the Lagrange multiplier v for each pixel. Calculate the derivative of objective function J with π_{ij} and set the result to zero.

$$\frac{\partial}{\partial \pi_{ij}} \left[J - \sum_{i=1}^{L} v \left(\sum_{j=1}^{K} \pi_{ij} - 1 \right) \right] = -\frac{z_{ij}}{\pi_{ij}} - v \tag{27}$$

From the above, the estimation of prior π_{ij} is given by

$$\pi_{ij}^{(t+1)} = z_{ij}^{(t)} \Big/ \sum_{k=1}^{K} z_{ik}^{(t)} \tag{28}$$

The computation process of APDE-GMM is summarized as:

1. Initialize: label K, step Δt, mean μ_j, covariance Σ_j, and prior π_{ij}.
2. Compute the estimated image u_{mn} using (21)
3. E-step: Calculate the posterior probability z_{ij} by (14)
4. M-step: Update parameters μ_j, Σ_j, and π_{ij} using (24), (26), and (28), respectively.
5. Check the convergence of the objective function J in terms of (16). If the converging condition is not satisfied, we need to go back to step 2 and recalculate the value of objective function J until it converges.

When the objective function J converges, the label Ω_j of each pixel x_i can be obtained by calculating the posterior probability z_{ij}, and then the image segmentation can be completed. Each pixel x_i satisfies the following conditions:

$$x_i \in \Omega_j : \text{IF } z_{ij} \geq z_{ik};\ j,\ k = (1,\ 2,\ \ldots,\ K) \tag{29}$$

5 Experiments

In this section, the evaluation of APDE-GMM is conducted using three synthetic images (256 × 256 pixels) and twenty IV-OCT images from nine CAD patients (eight males and one female). These IV-OCT images (300 × 300 pixels) were collected by a C7 model OCT scanner (St. Jude Medical, USA), which was provided by the Department of Cardiology at Peking Union Medical College Hospital, China. The plaque areas of some typical lesion images are manually labeled by cardiologists in this hospital as the ground truth. With regard to the experimental environment, the hardware environment is 2.30 GHz Intel Core i5-6300HQ CPU, NVIDIA GeForce GTX 960M GPU, and 8.00 GB DDR4 memory, and the software environment is Windows 10 operating system and MATLAB 2016a software. For comparison, the following several metrics are involved: (a) Misclassification Ratio (MCR), Jaccard Similarity (JS), Dice Similarity Coefficient (DISC) and Probabilistic Rand Index (PRI).

MCR calculates the proportion of misclassified pixels in total pixels, which is defined below:

$$\text{MCR} = \frac{\text{number of misclassified pixels}}{\text{total number of pixels}} \times 100 \tag{30}$$

MCR takes its value between 0 and 100, while the closer the MCR value is to zero, the more the segmentation result approaches to the ground truth.

DISC provides another similarity measurement of two sample sets.

$$\text{DISC} = \frac{2\text{TP}}{2\text{TP} + \text{FN} + \text{FP}} \times 100 \tag{31}$$

where TP is the number of true positives, FN is the number of false negatives and FP is the number of false positives. DISC ranges from 0 to 100, while a higher value indicates better performance.

JS is a statistic used for testing the similarity. It applies the overlap degree between the segmentation result and the actual to evaluate the algorithm performance.

$$\mathrm{JS} = \frac{\left|S_{\mathrm{seg}} \bigcap S_{\mathrm{gt}}\right|}{\left|S_{\mathrm{seg}} \bigcup S_{\mathrm{gt}}\right|} \tag{32}$$

where S_{seg} and S_{gt} stand for segmentation result and ground truth, respectively. JS takes value between 0 and 1, the closer JS is to 0, the poorer the segmentation result is.

Next, we adopt PRI to compare the similarity of two different ways.

$$\mathrm{PRI}=\frac{1}{L(L-1)}\sum_{i=1}^{m}\sum_{j=1}^{n}\left[c_{ij}\,p_{ij}+(1-c_{ij})(1-p_{ij})\right] \tag{33}$$

where L is the number of observations. If pixel i and j belong to the same class in evaluated image, the value of c_{ij} is one. Otherwise, its value is zero. p_{ij} is the ground truth probability that pixel i and j belong to the same class. PRI value ranges from 0 to 1, while a smaller value represents a more accurate segmentation result.

5.1 Effect of parameters α and β in diffusivity function

According to (11) and (12), the gradient threshold $\eta(u)$ is proportional to diffusivity function $\phi(s)$. Therefore, in order to satisfy the requirement of $\phi(s)$, we need to choose the appropriate parameters α and β for $\eta(u)$. We first discuss the influence of two parameters α and β on the $\eta(u)$. Figure 3 displays the plots of diffusivity function $\phi(s)$ with different values of α and β. When both α and β are smaller, $\eta(u)$ will be smaller in the whole iteration. On the contrary, $\eta(u)$ will remain larger throughout the iteration. Therefore, from Fig. 3, it can be seen that the first choice ($\alpha = 0.2, \beta = 0.02$) led to weak smoothing effect on its early iterations among all the test cases. For the results obtained with the sixth set ($\alpha = 1, \beta = 0.1$), we found the heavy denoising performance may be carried out throughout the iteration process. It is because, in this case, a larger value is assigned to diffusivity function $\phi(s)$. Based on the above results, we noted that the diffusivity function $\phi(s)$ might provide a relatively better denoising properties while we take α from 0.4 to 0.6, and β set its value in $[0.04, 0.06]$. This is the reason why we set parameters $\alpha = 0.5$ and $\beta = 0.05$ in the following experiments.

5.2 Experiments with synthetic images

To test the behavior of APDE-GMM, the experiment is first conducted on three synthetic images with different levels of

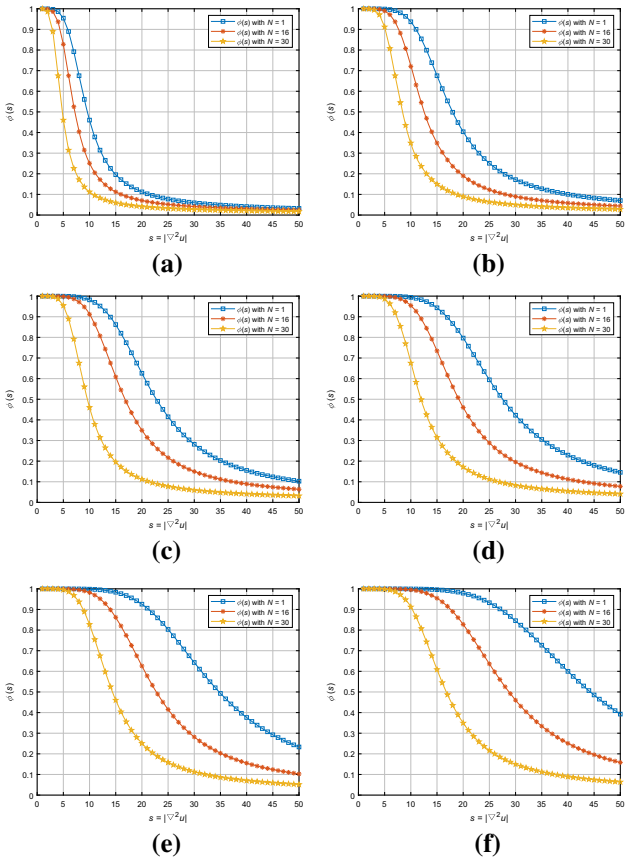

Fig. 3 The proposed adaptive diffusivity function, **a** $\alpha = 0.2$, $\beta = 0.02$; **b** $\alpha = 0.4$, $\beta = 0.04$; **c** $\alpha = 0.5$, $\beta = 0.05$; **d** $\alpha = 0.6$, $\beta = 0.06$; **e** $\alpha = 0.8$, $\beta = 0.08$; **f** $\alpha = 1.0$, $\beta = 0.1$

complexity, which is illustrated in Fig. 4. We would like to compare the performance with several existing algorithms based on the model of clustering or FMM. In this regard, this paper considers the standard GMM [19], FCM [20], SMM [21], fast and robust spatially constrained Gaussian mixture model (FRSCGMM) [22] and fourth-order PDE-based fuzzy c-means (AFPDEFCM) [16]. For all of these approaches, the same iterations are used. The first row demonstrates original images corrupted by speckle noise (intensity 5%). The proposed APDE-GMM results are compared with those produced by the above-mentioned algorithms shown in Fig. 4. All approaches can successfully label these images. However, we also observe that noise is still in the results obtained using GMM, SMM and FCM. They might not consider the spatial relationship between neighboring pixels. FRSCGMM removes noise effectively, but the visual effect of the edge seems too smooth. Besides, the segmentation result also indicates that AFPDEFCM is efficient in dealing with noise. This could be because of the use of Y–K diffusivity function. From Fig. 4, we can conclude that the APDE-GMM outperforms the other comparison approaches in the quality of image. It

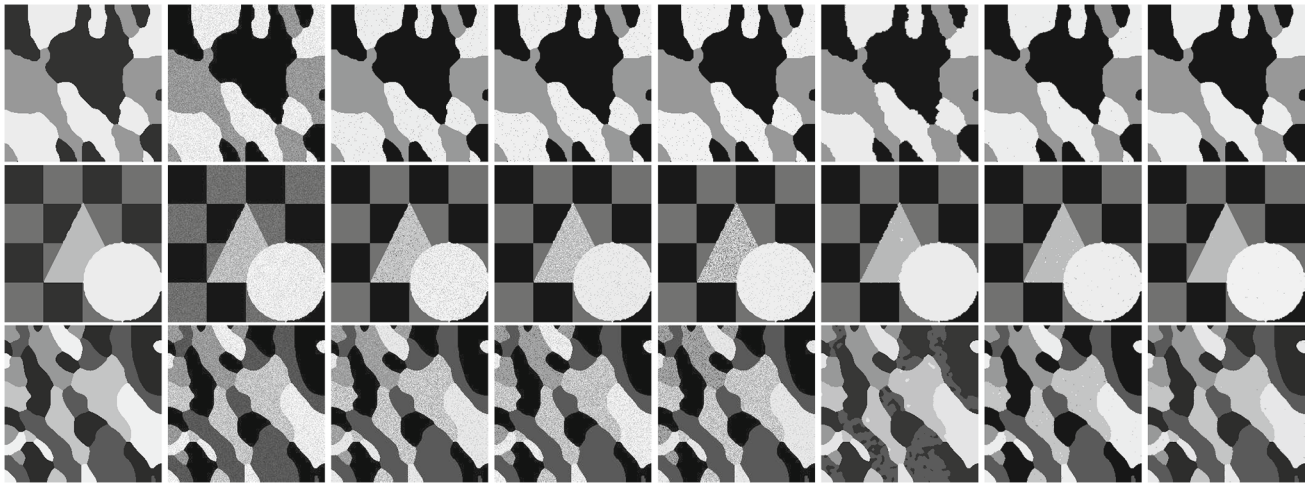

Fig. 4 Segmentation results for synthetic images. From the first column to the last is original images, noisy images (speckle noise: intensity 5%), FCM, GMM, SMM, FRSCGMM, AFPDEFCM, and APDE-GMM, respectively

Table 1 PRI obtained by applying six algorithms, the last column is mean and standard deviation (mean ± SD)

Methods	Image 1	Image 2	Image 3	Mean ± SD
FCM	0.9677	0.9508	0.9354	0.9513 ± 0.0161
GMM	0.9759	0.9714	0.9381	0.9618 ± 0.0206
SMM	0.9792	0.9724	0.9405	0.9640 ± 0.0207
FRSCGMM	0.9989	0.9825	0.9648	0.9821 ± 0.0171
AFPDEFCM	0.9986	0.9941	0.9816	0.9914 ± 0.0088
APDE-GMM	0.9991	0.9963	0.9847	0.9933 ± 0.0076

Table 2 MCR obtained by applying six algorithms, the last column is mean and standard deviation (mean ± SD)

Methods	Image 1	Image 2	Image 3	Mean ± SD
FCM	2.6489	7.5363	13.9206	8.0352 ± 5.6523
GMM	1.9516	5.3848	13.5590	6.9651 ± 5.9628
SMM	1.6800	5.0892	12.8605	6.5432 ± 5.7303
FRSCGMM	0.0760	1.4040	4.0505	1.8435 ± 2.0233
AFPDEFCM	0.1068	0.6051	2.3199	1.0106 ± 1.1609
APDE-GMM	0.0732	0.5081	1.3779	0.6530 ± 0.6643

reduces the effect of noise significantly. This may be due to the application of adaptive diffusion function.

To test the performance of a model, only visual comparison is not enough and the segmentation results need to be evaluated through quantitative metrics. Here, two quality assessment metrics PRI and MCR are implemented to evaluate the difference between the ground truth and the segmented results. The results are listed in Tables 1 and 2. One can discover that PRI stays above 0.9847 to all test images, which confirm the efficiency of the APDE-GMM. In addition, FCM, GMM and SMM get the poor results in terms of

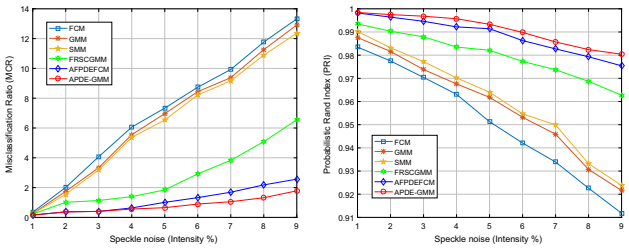

Fig. 5 MCR and PRI obtained by some models under different noise environment, (left) MCR and PRI (right)

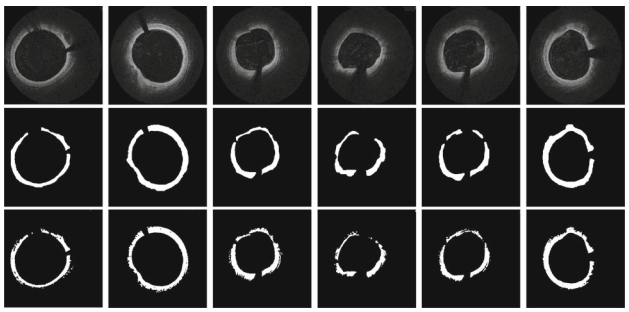

Fig. 6 The APDE-GMM segmentation results, from the first row to the last is original images, ground truth and segmentation results

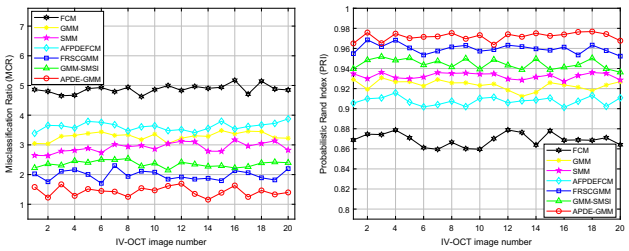

Fig. 7 MCR and PRI obtained by some approaches for twenty IV-OCT images, (left) MCR and PRI (right)

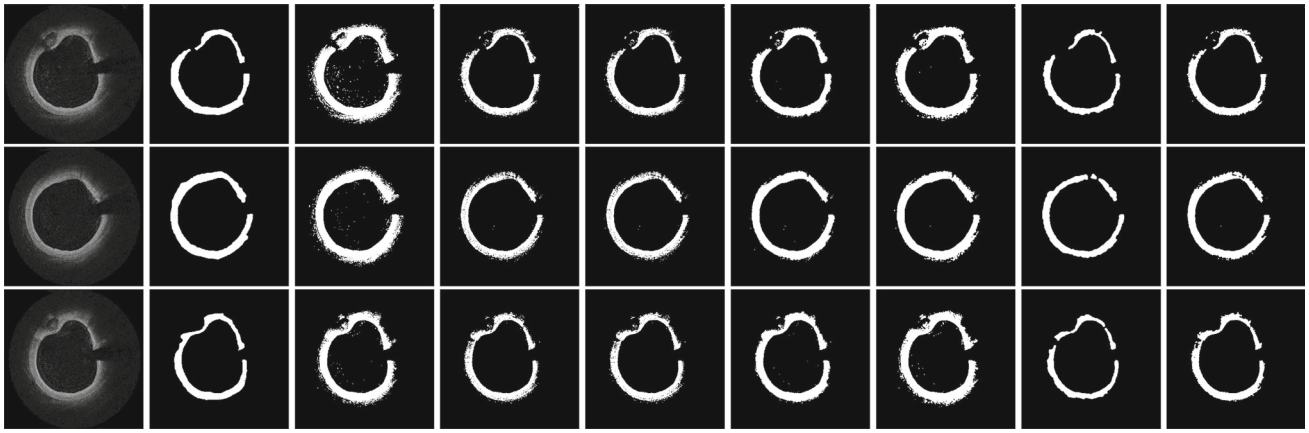

Fig. 8 Segmentation results for IV-OCT images. From the first column to the last is original images, ground truth, FCM, GMM, SMM, FRSCGMM, AFPDEFCM, GMM-SMSI and APDE-GMM, respectively

PRI and MCR. MCR values of our method can remain more stable and lower than the other methods.

To compare APDE-GMM with the above methods, the influence of different noise levels on them is discussed. Figure 5 displays the average MCR and PRI of three images for all approaches. The intensity of speckle noise ranges from 1 to 9%. It can be found that the AFPDEFCM with Y–K diffusivity function performs better than those of FRSCGMM. However, the latter is more robust to speckle noise than FCM, GMM, and SMM. In addition, as evident from Fig. 5, the APDE-GMM outperforms other methods with the lowest MCR. It is due to the fact that this method applies an adaptive diffusivity function as well as statistics-based GMM, which is able to model the intensity distribution of an image more accurately. Hence, based on all results reported by this experiment, we can preliminarily summarize that the APDE-GMM achieves better segmentation results.

5.3 Experiments with IV-OCT images

In this subsection, we first conduct the application of the APDE-GMM on clinical IV-OCT images, and some of corresponding results are given in Fig. 6. The images in the first and second rows are original images, and ground truth, respectively. It can be observed that our approach detects accurately the fibrotic plaque from vessel lumen of coronary artery. This is due partly to the fact that adaptive diffusivity function provides better noise removal and edge preservation, so that our method can overcome the effect of heavy speckle noise on the results. Besides, to quantitatively assess the performance of APDE-GMM, this experiment also investigates the performance of GMM with spatial information extracted from saliency map (GMM-SMSI) [23], which considers the spatial relationship between pixels. All these methods are evaluated on twenty IV-OCT images. The results are depicted in Fig. 7. We have found that APDE-GMM performs very well for the

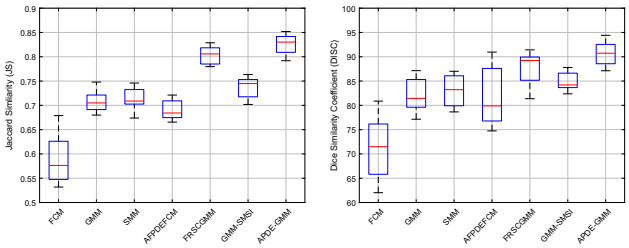

Fig. 9 JS and DISC obtained by some approaches for twenty IV-OCT images, (left) JS and DISC (right)

fibrotic plaque segmentation. Also, the performance of both GMM-SMSI and FRSCGMM is better, but not significant, compared to the SMM and GMM. With respect to MCR and PRI values, it should be remarked that FCM provides poor performance.

The last experiment provided here is to demonstrate the accuracy of the APDE-GMM for various lesion IV-OCT images, and experiments are carried out on twenty IV-OCT images using our model compared with other methods. Figure 8 exhibits a visual comparison of partial segmentation results. We can observe that our method gives competitive results for these test images. The results indicate that the APDE-GMM can maintain a good balance between edge preservation and image denoising. To further investigate the advantages of APDE-GMM in detecting fibrotic plaque, this paper gives quantitative analysis in terms of JS and DISC, and results are illustrated in Fig. 9. By comparing, the performance of our model is still better than other six approaches.

6 Conclusions

This paper presented an unsupervised IV-OCT image segmentation approach based on GMM and the fourth-order PDE. In this scheme, an adaptive diffusivity function was

incorporated into PDE, so that our method can effectively remove high-level speckle noise. The proposed APDE-GMM achieved accurate IV-OCT image segmentation compared with well-known algorithms, and results proved that APDE-GMM may assist doctor in diagnosis of CAD. Future work will improve the proposed model in order to separate various types of plaque better, such as calcified plaque.

Acknowledgements The authors would like to thank the anonymous reviewers and the associate editor for their insightful comments that significantly improved the quality of this paper. This work was supported by the National Nature Science Foundation of China under Grant 61872143.

References

1. Zahnd, G., Hoogendoorn, A., Combaret, N., et al.: Contour segmentation of the intima, media, and adventitia layers in intracoronary OCT images: application to fully automatic detection of healthy wall regions. Int. J. Comput. Assist. Radiol. Surg. **12**, 1923–1936 (2017)
2. Guo, X., Tang, D., David, M., et al.: A machine learning-based method for intracoronary OCT segmentation and vulnerable coronary plaque cap thickness quantification. Int. J. Comput. Methods **15**(1), 1–12 (2018)
3. Xu, M., Cheng, J., Wong, D.W.K.: Automatic image classification in intravascular optical coherence tomography images. In: Proceedings of IEEE Region 10 Conference (TENCON), pp. 1544–1547 (2016)
4. Celi, S., Berti, S.: In-vivo segmentation and quantification of coronary lesions by optical coherence tomography images for a lesion type definition and stenosis grading. Med. Image Anal. **18**(7), 1157–1168 (2014)
5. Xu, M., Cheng, J., Li, A., et al: Fibroatheroma identification in intravascular optical coherence tomography images using deep features. In: Proceedings of Annual International Conference of the IEEE Engineering in Medicine and Biology Society, pp. 1501–1504 (2017)
6. Ji, Z., Huang, Y., Xia, Y., et al.: A robust modified Gaussian mixture model with rough set for image segmentation. Neurocomputing **266**, 550–565 (2017)
7. Cheriyan, M.M., Prawin, A.M., Kumar, A.: Blind source separation with mixture models—a hybrid approach to MR brain classification. Magn. Reson. Imaging **54**, 137–147 (2018)
8. Banerjeel, A., Maji, P.: Constrained Students' t-distribution based mixture model for robust image segmentation. J. Math. Imaging Vis. **60**(3), 355–381 (2018)
9. Liu, Z., Song, Y., Xie, C., et al.: A new clustering method of gene expression data based on multivariate Gaussian mixture models. Signal Image Video Process. **10**(2), 359–368 (2016)
10. Ahmadvand, A., Kabiri, P.: Multispectral MRI image segmentation using Markov random field model. Signal Image Video Process. **10**(2), 251–258 (2016)
11. Barbu, T.: Nonlinear fourth-order hyperbolic PDE-based image restoration scheme. In: Proceedings of IEEE International Conference on e-Health and Bioengineering, pp. 19–21 (2015)
12. Barbu, T.: A hybrid nonlinear fourth-order PDE-based image restoration approach. In: Proceedings of International Conference on System Theory, Control and Computing, pp. 754–756 (2016)
13. Barbu, T.: Additive noise removal using a nonlinear hyperbolic PDE-based model. In: Proceedings of International Conference on Development and Application Systems, pp. 1–5 (2018)
14. Heydari, M., Karami, M.R., Babakhani, A.: A new adaptive coupled diffusion PDE for MRI Rician noise. Signal Image Video Process. **10**(7), 1212–1218 (2016)
15. Soorajkumar, R., Kumar, P.K., Girish, D.R., et al: Fourth order PDE based Ultrasound despeckling using ENI classification. In: Procedings of International Conference on Signal Processing and Communication, pp. 1–5 (2016)
16. Kumar, R., Srivastava, S., Srivastava, R.: A fourth order PDE based fuzzy c-means approach for segmentation of microscopic biopsy images in presence of poisson noise for cancer detection. Comput. Methods Programs Biomed. **146**, 59–68 (2017)
17. Schmitt, J.M.: Optical coherence tomography (OCT): a review. IEEE J. Sel. Top. Quantum Electron. **5**(4), 1205–1215 (1999)
18. You, Y.L., Kaveh, M.: Fourth-order partial differential equations for noise removal. IEEE Trans. Image Process. **9**(10), 1723–1730 (2000)
19. Titterington, D.M., Smith, A.F.M., Makov, U.E.: Statistical Analysis of Finite Mixture Distributions. Wiley, Hoboken (1985)
20. Trivedi, M.M., Bezdek, J.C.: Low-level segmentation of aerial images with fuzzy clustering. IEEE Trans. Syst. Man Cybern. **16**(4), 589–598 (1986)
21. Sfikas, G., Nikou, C., Galatsanos, N.: Robust image segmentation with mixtures of Student's-t distributions. In: Proceedings of IEEE International Conference on Image Processing, pp. 273–276 (2007)
22. Nguyen, T.M., Wu, Q.M.J.: Fast and robust spatially constrained Gaussian mixture model for image segmentation. IEEE Trans. Circuits Syst. Video Technol. **23**(4), 621–635 (2013)
23. Bi, H., Tang, H., Yang, G., et al.: Accurate image segmentation using Gaussian mixture model with saliency map. Pattern Anal. Appl. **21**(3), 869–878 (2018)